

Transverse phase space reconstruction study in Shanghai soft X-ray FEL facility

Qing-Lin Yu^{1,2} · Duan Gu¹ · Meng Zhang¹ · Ming-Hua Zhao¹

Received: 19 July 2017 / Revised: 24 September 2017 / Accepted: 1 November 2017 / Published online: 22 December 2017
© Shanghai Institute of Applied Physics, Chinese Academy of Sciences, Chinese Nuclear Society, Science Press China and Springer Nature Singapore Pte Ltd. 2017

Abstract Phase space is one of the most important parameters used to describe beam properties. Computer tomography, as a method for reconstructing phase space and measuring beam emittance, has been used in many accelerators over the past few decades. In this paper, we demonstrate a transverse phase space reconstruction study in the Shanghai soft X-ray free electron laser facility. First, we discuss the basic principles of phase space reconstruction and the advantage of reconstructing beam distribution in normalized phase space. Then, the phase space reconstruction results by different computer tomography methods based on the maximum entropy (MENT) algorithm and the filtered back projection algorithm in normalized phase space are presented. The simulation results indicate that, with proper configuration of the phase advance between adjacent screens, the MENT algorithm is feasible and has good efficiency. The beam emittance and Twiss parameters are also calculated using the reconstructed phase space.

Keywords Emittance · Phase space reconstruction · MENT algorithm · SXFEL

1 Introduction

Over the past few decades, the computer tomography method has been used in accelerators to characterize the phase space of the particle beam. The tomography section of the Deutsches Elektronen Synchrotron's Photo Injector Test Facility at Zeuthen (PITZ) [1, 2] consists of three FODO structures and four screens for measuring the transverse profile of the beam. In this process, the maximum entropy (MENT) [3–5] algorithm was used to reconstruct the phase space of the beam. In the Accelerators and Lasers in Combined Experiments (ALICE) accelerator [6], three screens with FODO cells have been used. The Paul Scherrer Institute (PSI) and the Spallation Neutron Source (SNS) [7] also use three to five screens to achieve phase space reconstruction using the MENT algorithm. In the accelerator in TRIUMF [8], a wire scanner with a quadrupole is used instead of screens. Three wires, fixed at three angles, are used to measure the projections in the transverse space, and MENT is used for the reconstructions. In the University of Maryland Electron Ring (UMER) [9], the strengths of a few quadrupoles are adjusted to obtain the full 180° range of angles. The reconstruction is carried out using a filtered back projection (FBP) algorithm. In ALICE, the FBP algorithm [9–11] is also used to reconstruct the phase space of the beam.

The preliminary construction of the Shanghai soft X-ray free electron laser (SXFEL) facility has been completed, and it is currently under commissioning. The main linear accelerator (LINAC) accelerates the beam to an energy of 840 MeV. The local energy spread is 0.1–0.15%, the peak current is ~ 600 A, the bunch charge is 0.5 nC, and the normalized emittance is about 2 mm mrad [12]. In order to verify the phase space reconstruction scheme, we use the

✉ Ming-Hua Zhao
zhaominghua@sinap.ac.cn

¹ Shanghai Institute of Applied Physics, Chinese Academy of Sciences, Shanghai 201800, China

² University of Chinese Academy of Sciences, Beijing 100049, China

ELEGANT code [13] to simulate the proposed procedures. During the simulation, both the FBP algorithm and the MENT algorithm are used to reconstruct the phase space at the B11 segment of the SXFEL facility. In addition, the beam emittance and Twiss parameters are calculated as well.

2 Basic principles

2.1 Computer tomography

Briefly, the concept of computer tomography is to use the projections of an object at different angles to calculate the two-dimensional density distribution of the object. The image reconstruction algorithm is divided into two categories: one is an analysis reconstruction algorithm, which is based on the Radon transform, and the other is an iterative reconstruction algorithm mainly used to solve equations.

The FBP algorithm is a type of analysis reconstruction algorithm, and it has been widely used in image reconstruction. This algorithm is based on the Fourier slice theorem and it applies the inverse Radon transformation for image reconstruction. Considering the axes (s, t) rotated by angle θ in Fig. 1, the coordinates are related to (x, y) by

$$\begin{cases} s = x \cos \theta + y \sin \theta \\ t = -x \sin \theta + y \cos \theta \end{cases} \quad (1)$$

Assuming that the density function of the object is $f(x, y)$, the projection of the object at an angle θ is $p_\theta(s)$, as shown in Fig. 1.

The projection of the object at angle θ is

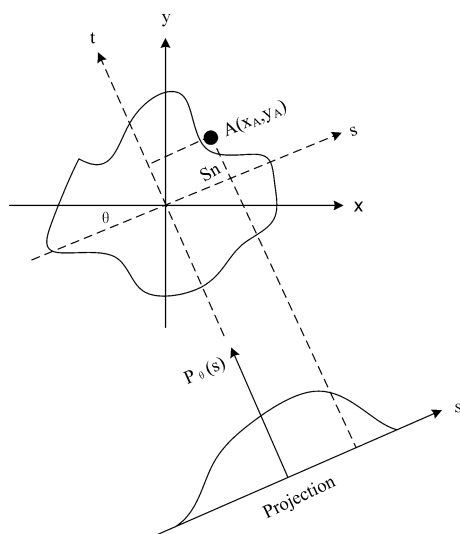


Fig. 1 Projection of the object at projection angle θ

$$P_\theta(s) = \int_{-\infty}^{\infty} f(x, y) dt. \quad (2)$$

The one-dimensional Fourier transform of the projection is

$$S_\theta(\omega) = \int_{-\infty}^{\infty} P_\theta(s) e^{-i2\pi\omega s} ds, \quad (3)$$

where ω is the angular frequency in the frequency domain. By substituting Eq. (2) into Eq. (3) and applying the two-dimensional Fourier transform, the density distribution function of the object can be obtained as

$$f(x, y) = \int_0^\pi \left[\int_{-\infty}^{\infty} S_\theta(\omega) |\omega| e^{i2\pi\omega s} d\omega \right] d\theta. \quad (4)$$

Therefore, as long as the projections of the object at different angles are obtained, the density function can be calculated.

The MENT algorithm is a type of iterative reconstruction algorithm. The main purpose of the algorithm is to determine the unknown function $h_n(s_n(x_A, y_A))$. This function is defined by the conditions for the stationary solution of the Lagrange equation related to the density distribution of the particles. Variable s denotes the distance from point A to axis t , as shown in Fig. 1, and n represents the n th projection. The density function can be represented by the following unknown function:

$$f(x, y) = \prod_{n=1}^N h_n(s_n(x_A, y_A)). \quad (5)$$

By substituting Eq. (5) into Eq. (2), we obtain:

$$p_n(s) = h_n(s) \int \prod_{k \neq n}^N h_k(s_k(x_A, y_A)) dt. \quad (6)$$

Equation (6) can be solved for the unknown $h_n(s)$ by using a technique known as Gauss–Seidel iteration; thus, the density distribution function $f(x, y)$ [5] can be obtained.

The specific steps are as follows:

1. For all n , set the initial value of $h_n(s)$ to the constant value of 1.
2. For each n , use Eq. (6) and the measured $p_n(s)$ to calculate $h_n(s)$.
3. Projection $p_n(s)$ can be calculated by Eqs. (5) and (2) using $h_n(s)$ in step 2.
4. Compare this calculated $p_n(s)$ with the measured $p_n(s)$.
5. Repeat the above steps (except for the step 1) until the difference between the two values in step 4 is very small.

After several iterations, the error reduces to the permitted range, and the objective function is obtained. For the

MENT algorithm, usually only three to five projections are required to reconstruct the phase space.

2.2 Principle of phase space reconstruction

When the electron beam passes through the quadrupole, the drift space, or other components, the bunch is rotated, stretched, and sheared. The transverse projected image of the beam can be obtained by the yttrium aluminum garnet (YAG) or optical transition radiation (OTR) screen after the quadrupole, and the projections of the phase space can be obtained by integrating the image along the x -axis. By changing the strength of the quadrupole, the projections of the beam at different angles can be obtained, or other methods can be used (such as varying the length of the drift space) to obtain the projections at different angles, which are used for the phase space reconstruction.

Assuming that the electron beam is transformed from reconstruction location A to observation location B , the transfer matrix is

$$\begin{pmatrix} x_B \\ x'_B \end{pmatrix} = \begin{pmatrix} R_{11} & R_{12} \\ R_{21} & R_{22} \end{pmatrix} \begin{pmatrix} x_A \\ x'_A \end{pmatrix}. \tag{7}$$

The effect of this mapping is a geometrical transformation, as shown in Fig. 2. The two parallel lines 1 and 2 in Fig. 2a correspond to lines 1 and 2 in Fig. 2b.

The image obtained at B denotes the particle density distribution on the xy -plane; however, the distribution function needs to be on the xx' -plane. If the image intensity is integrated along the y -direction at each x -value, the result is the same as the projection in the phase space, as in each case we are effectively counting the number of particles within a narrow range of x -coordinate values. Then, the transfer matrix in Eq. (7) is used to obtain the projection at reconstruction point A [14] as

$$P_A(s) = \rho P_B(x_B), \tag{8}$$

where ρ is the scaling factor and using

$$\tan \theta = \frac{R_{12}}{R_{11}}. \tag{9}$$

It can be expressed as

$$\rho = \sqrt{R_{11}^2 + R_{12}^2}, \tag{10}$$

$$s = \frac{x_B}{\rho}, \tag{11}$$

where s is the distance from line 1 to the origin, as shown in Fig. 2a. With the projections of phase space known at different angles at point A , the phase space can be reconstructed using the algorithms described above.

2.3 Normalized phase space

In general, the shape of the phase space distribution is long and narrow, as in the case when the beam passes through the long drift space, since it stretches and shears the transverse phase space distribution of the bunch. According to Liouville’s theorem, in order to keep the area of the phase space unchanged, the phase space of the beam has to be narrowed. As a result, most particles would lie along a particular direction. Sampling in this distribution at a uniform interval of angles can lead to a distortion in reconstruction.

However, in normalized phase space, the distribution of the phase space is a circle (unless the electron beam is “distorted” by certain effects). The reason is that in normalized phase space, the Twiss parameters $\beta = 1$ and $\alpha = 0$. This corresponds to a distribution, where the correlation $\langle x_N, x'_N \rangle = 0$. However, the correlation of a long and a narrow distribution cannot be zero, as its shape indicates a strong dependency on a certain direction. This means that the distribution can be apparently circular. If the particles are distributed symmetrically along two perpendicular straight lines, the correlation of this distribution is also zero. However, for the particle beam, the distribution may spread over all 360°. Sampling over angles uniformly in a circular distribution is more accurate. Therefore, reconstructing in the normalized phase space is better [15].

The relationship between normalized phase space and real phase space is:

$$\begin{pmatrix} x \\ x' \end{pmatrix} = \begin{pmatrix} \sqrt{\beta} & 0 \\ -\frac{\alpha}{\sqrt{\beta}} & \frac{1}{\sqrt{\beta}} \end{pmatrix} \begin{pmatrix} x_N \\ x'_N \end{pmatrix}, \tag{12}$$

where α and β are the Twiss parameters and subscript N denotes the normalized phase space. By adding Eq. (12) to the right-hand side of Eq. (7), the transfer matrix \tilde{R} required for the reconstruction in normalized phase space can be obtained as

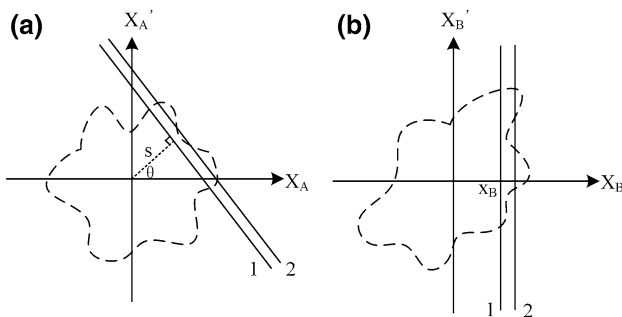


Fig. 2 Phase space distribution at a reconstruction location and b measurement location

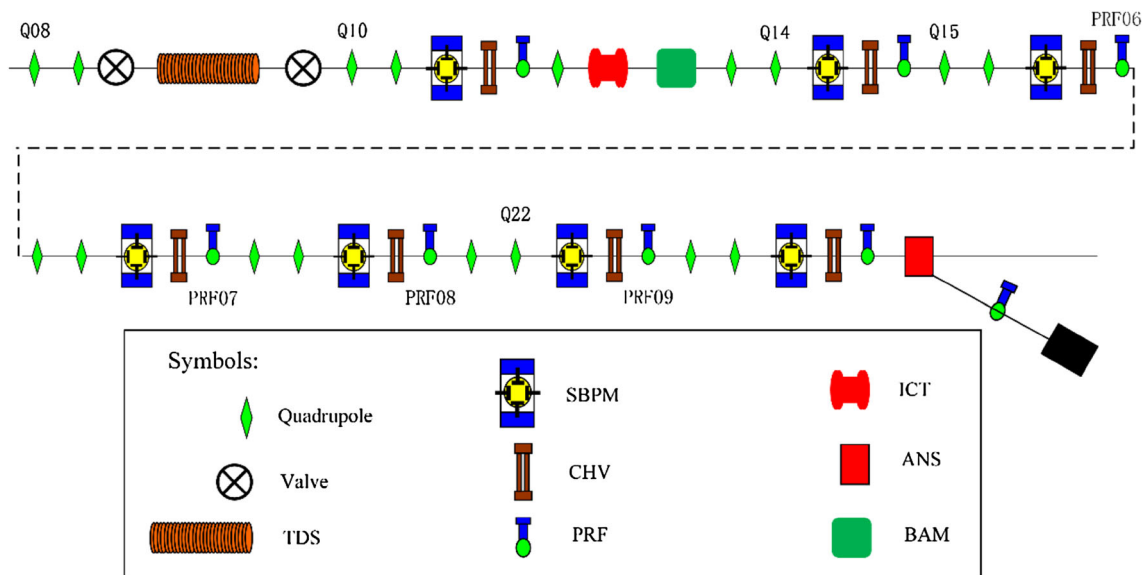


Fig. 3 (Color online) Schematic of a part of the structure of the BI1 section in the SXFEL facility

$$\tilde{R} = \begin{pmatrix} R_{11} & R_{12} \\ R_{21} & R_{22} \end{pmatrix} \begin{pmatrix} \sqrt{\beta_A} & 0 \\ -\frac{\alpha_A}{\sqrt{\beta_A}} & 1 \\ \sqrt{\beta_A} & \sqrt{\beta_A} \end{pmatrix}. \tag{13}$$

With further calculation the transfer matrix can be rewritten as follows:

$$\tilde{R} = \begin{pmatrix} \sqrt{\beta_B} & 0 \\ -\frac{\alpha_B}{\sqrt{\beta_B}} & 1 \end{pmatrix} \begin{pmatrix} \cos \mu & \sin \mu \\ -\sin \mu & \cos \mu \end{pmatrix}. \tag{14}$$

Here, the subscript *B* denotes the Twiss parameters corresponding to position *B*, and μ is the phase advance. According to the formula in Eq. (14), the formulas in Eqs. (9) and (10) can be used to obtain the projection angle and ρ in normalized phase space:

$$\begin{cases} \tan \theta = \frac{\tilde{R}_{12}}{\tilde{R}_{11}} = \tan \mu \\ \rho = \sqrt{\tilde{R}_{11}^2 + \tilde{R}_{12}^2} = \sqrt{\beta_B} \end{cases}. \tag{15}$$

It can be seen that in normalized phase space, the projection angle is equal to the phase advance. The projections can be obtained using the formulas in Eqs. (8) and (11). Therefore, reconstruction in the normalized phase space is possible.

3 Simulation and analysis

3.1 Design of the program

The schematic of the BI1 section of the SXFEL facility is shown in Fig. 3. The entrance of Q8 was chosen as the

reconstruction location. Quadrupoles Q10–Q14 were used to match the following four FODO cells.

The beam energy of this section was 256 MeV in the simulation. With the appropriate quadrupole strength from Q15 to Q22, the phase advance from one screen to the next was set to 45°. From Eq. (14), the projection angle in normalized phase space is known to be 45°. Thus, the projections obtained from the four screens could cover the entire 180° range. We used the MENT algorithm and the FBP algorithm to reconstruct the normalized phase space.

Table 1 lists the positions and phase advance values of the profile (PRF) 06–09. It can be seen in Table 1 that the interval of phase advances between each screen is almost 45°. Figure 4 shows the β function and phase advance in the *x*-direction in the BI1 section. The phase advance in the *x*-direction is denoted by ψ_x .

3.2 Simulation and reconstruction

Combined with the parameters of the SXFEL facility, we used the ELEGANT code to simulate the propagation of the electron beam and then performed phase space reconstruction. According to the principles in Sect. 2, the phase space reconstruction process is as follows:

1. Generating the original electron beam based on the design and parameters of the SXFEL.

Table 1 Positions and phase advances of PRF06–09

	PRF06	PRF07	PRF08	PRF09
Position (m)	8.515	10.315	12.115	13.915
Phase advance (°)	100.018	145.019	190.023	235.023

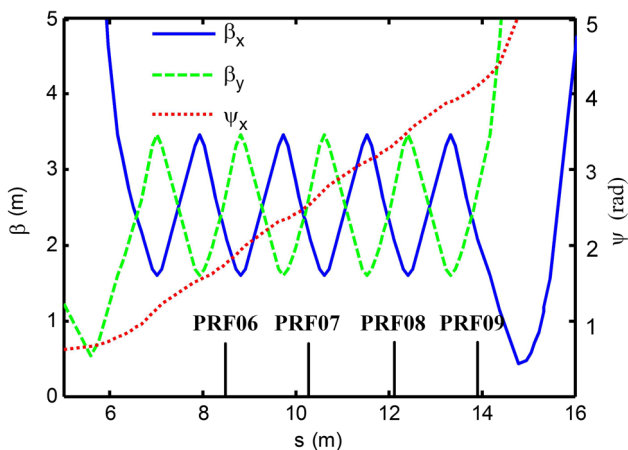


Fig. 4 (Color online) β Function and phase advance in the x -direction in the B11 section

2. Obtaining beam images on screens 6–9.
3. Calculating the projections of the beam image along the x -direction at the four screens.
4. Reconstructing the normalized phase space of the beam at the entrance of Q8.
5. Transforming the image obtained from step 4 to the real phase space.
6. Calculating the emittance and Twiss parameters of the beam from the reconstructed phase space data.

Figure 5 shows the original phase space and the reconstructed phase space. The number of iterations and the reduction in errors by using the MENT algorithm are shown in Table 2. The errors refer to the relative errors between calculated $p_n(s)$ and measured $p_n(s)$.

In Fig. 5, the reconstructed phase space distribution obtained by the MENT algorithm (Fig. 5f) is very similar

Fig. 5 (Color online) Original and reconstructed phase space. **a** Original phase space, **b** projections at different angles. Reconstructed normalized phase space **(c)** and real phase space **(d)** by the FBP algorithm. Reconstructed normalized phase space **(e)** and real phase space **(f)** by the MENT algorithm

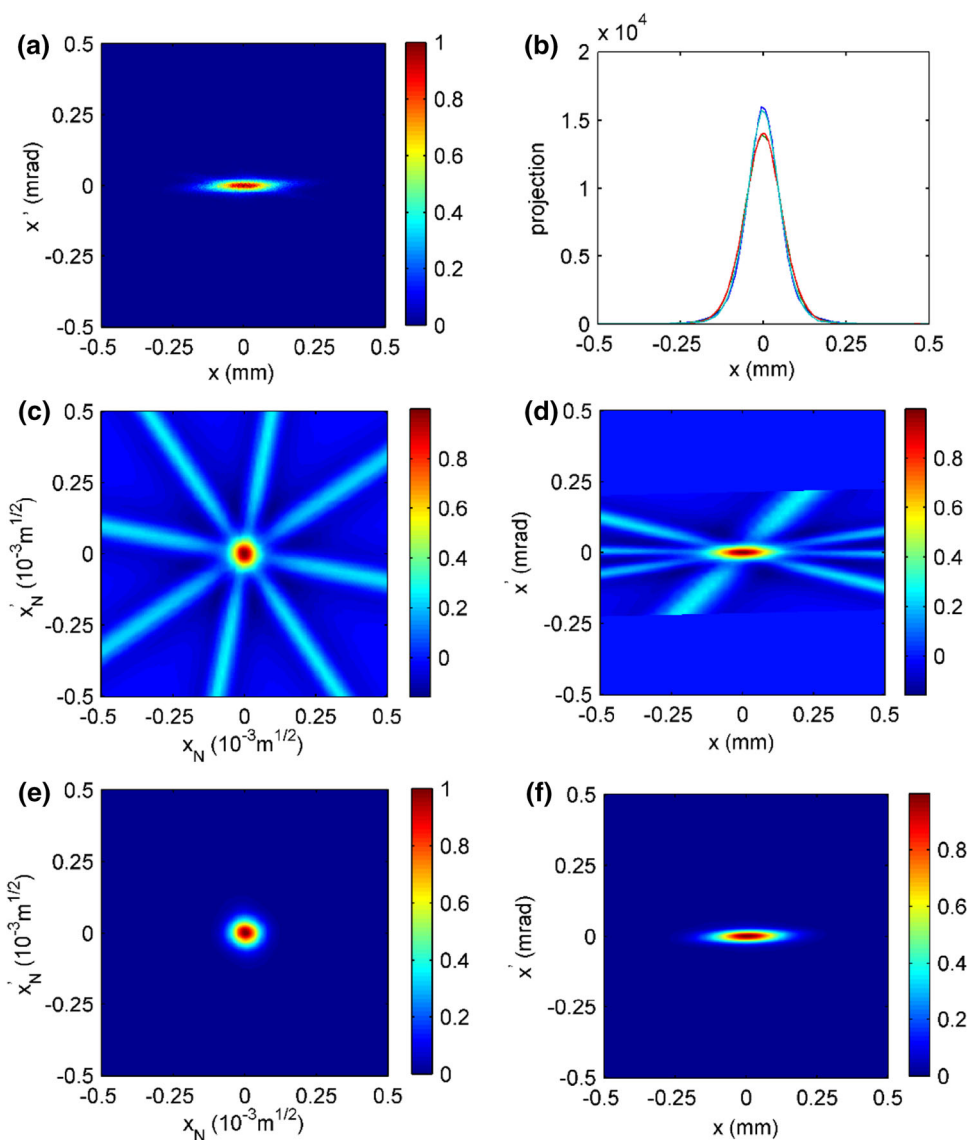


Table 2 Number of iterations and reduction in errors by using the MENT algorithm

Number of iterations	Error
0	39,163.356392
1	0.238430
2	0.063809
3	0.008181

Table 3 Measured values compared with the original values

	Original values	Measured values
α	- 0.1346	- 0.0769
β	5.471	5.481
Normalized emittance (mm mrad)	0.987	0.860

to the original phase space distribution. However, there are severe artifacts of the reconstructed phase space distribution obtained by FBP algorithm (Fig. 5d). According to the theory of the FBP algorithm, the object function $f(x, y)$ is the cumulative result of the filtered projections in the range of $\sim 0^\circ$ – 180° . In the simulation, we only use four projections of different angles; thus, the artifacts of Fig. 5d are very severe due to the insufficient projection data. The ideal condition for the FBP algorithm is to use enough projections, covering the full 180° . Furthermore, the top and bottom parts of Fig. 5d are significantly different from the middle part, which is due to the transformation of coordinates from the normalized phase space to the real phase space. Figure 5f shows that the MENT algorithm requires only a small number of projections (usually 3–5) to give an acceptable reconstruction result. Therefore, the FBP algorithm is applicable when there are more projections available, while the MENT algorithm can complete the reconstruction with a small amount of projections.

4 Results and discussion

The Twiss parameters and the emittance of the beam can be calculated by the following formulas [6]:

$$\langle x^2 \rangle = \beta \varepsilon, \quad (16)$$

$$\langle x'^2 \rangle = \gamma \varepsilon, \quad (17)$$

$$\langle xx' \rangle = -\alpha \varepsilon, \quad (18)$$

$$\varepsilon = \sqrt{\langle x^2 \rangle \langle x'^2 \rangle - \langle xx' \rangle^2}, \quad (19)$$

where $\langle \rangle$ denotes averaging and ε is the beam emittance. Table 3 shows the original values and the measured values calculated from the image data of Fig. 5f.

The values of α and β vary in the range of approximately -9.007 to 5.410 and ~ 0.11 – 28.18 , respectively, in the BI1 section. It can be seen that the measured values of the beam are very close to the original values.

The error mainly comes from the following issues: (1) in the simulation, the Twiss parameters of the beam did not accurately match with the Twiss parameters of the lattice structure. Particles did not travel along the ideal trajectory. (2) The interpolation method used to transform from the normalized phase to real phase space inevitably leads to an interpolation error. (3) The interpolation method was also used to calculate $h_n(s)$ by using Eq. (6). Furthermore, more projections can improve accuracy.

5 Conclusion

This paper describes the principles of beam phase space reconstruction. The FBP algorithm and the MENT algorithm are used to reconstruct the phase space of the beam by simulation. The reconstructed results show a good agreement with the input values. The results also show the feasibility and reliability of the reconstruction of the beam phase space in the SXFEL facility using the MENT algorithm. With the commissioning of the SXFEL facility, the relevant reconstruction experiment will be completed. The phase space reconstruction technique provides a new and more effective method for measuring the beam phase space of the SXFEL facility.

References

1. S. Rimjaem, G. Asova, J. Bähr et al., Measurements of transverse projected emittance for different bunch charges at PITZ, in *Proceedings of FEL2010, Malmö*, pp. 410–413
2. G. Asova, H.J. Grabosch, M. Gross et al., First results with tomographic reconstruction of the transverse phase space at PITZ, in *Proceedings of FEL2011, Shanghai*, pp. 543–546
3. G. Minerbo, MENT: a maximum entropy algorithm for reconstruction a source from projection data. *Comput. Vision Graph.* **10**, 48–68 (1979). [https://doi.org/10.1016/0146-664X\(79\)90034-0](https://doi.org/10.1016/0146-664X(79)90034-0)
4. C.T. Mottershead, Maximum entropy beam diagnostic tomography. *IEEE Trans. Nucl. Sci.* **32**, 1970–1972 (1985). <https://doi.org/10.1109/TNS.1985.4333784>
5. K.M. Hock, M.G. Ibson, A study of the maximum entropy technique for phase space tomography. *J. Instrum.* **8**, P02003 (2013). <https://doi.org/10.1088/1748-0221/8/02/P02003>
6. M.G. Ibson, K.M. Hock, D.J. Holder et al., ALICE tomography section: measurements and analysis. *J. Instrum.* **7**, P04016 (2012). <https://doi.org/10.1088/1748-0221/7/04/P04016>

7. D. Reggiani, M. Seidel, C.K. Allen, Transverse phase-space beam tomography at PSI and SNS proton accelerators, in *Proceedings of IPAC2010, Kyoto*, pp. 1128–1130
8. Y.N. Rao, R. Baartman, Transverse phase space tomography in TRIUMF injection beamline, in *Proceedings of IPAC2011, San Sebastian*, pp. 1144–1146
9. D. Stratakis, R.A. Kishek, H. Li et al., Tomography as a diagnostic tool for phase space mapping of intense partial beams. *Phys. Rev. Spec. Topics Accel.* **9**, 112801 (2006). <https://doi.org/10.1103/PhysRevSTAB.9.112801>
10. A.C. Kak, M. Slaney, G. Wang, Principles of computerized tomographic imaging. *Med. Phys.* **29**, 106–108 (2001). <https://doi.org/10.1137/1.9780898719277>
11. C.B. McKee, P.G. Oshea, J.M.J. Madey, Phase space tomography of relativistic electron beams. *Nucl. Instrum. Methods Assoc.* **358**, 264–267 (1995). [https://doi.org/10.1016/0168-9002\(94\)01411-6](https://doi.org/10.1016/0168-9002(94)01411-6)
12. D.Z. Huang, Q. Gu, M. Zhang et al., Design study of the linac of the Shanghai soft X-ray free electron laser facility, in *Proceedings of FEL 2012, Nara*, pp. 141–143
13. M. Borland, Elegant: a flexible SDDS-compliant code for accelerator simulation. *Adv. Photon Sour. LS-287*, 1–11 (2000). <https://doi.org/10.2172/761286>
14. K.M. Hock, M.G. Ibison, D.J. Holder et al., A review of beam tomography research at Daresbury Laboratory. *Nucl. Instrum. Methods Assoc.* (2013). <https://doi.org/10.1016/j.nima.2014.03.050>
15. K.M. Hock, M.G. Ibison, D.J. Holder et al., Beam tomography in transverse normalized phase space. *Nucl. Instrum. Methods Assoc.* **642**, 36–44 (2011). <https://doi.org/10.1066/j.nima.2011.04.002>